Acta Materialia 268 (2024) 119741

Contents lists available at ScienceDirect

Acta Materialia

journal homepage: www.elsevier.com/locate/actamat

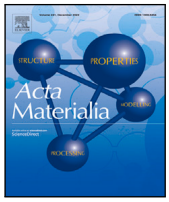

Full length article

Effect of Nb incorporation in Mo_2BC coatings on structural and mechanical properties — *Ab initio* modelling and experiment

Jaroslav Ženíšek [a,*], Pavel Souček [a], Pavel Ondračka [a], Zsolt Czigány [b], Vilma Buršíková [a], David Holec [c], Katalin Balázsi [b], Petr Vašina [a]

[a] Department of Plasma Physics and Technology, Masaryk University, Kotlářská 2, Brno 61137, Czech Republic
[b] Institute of Technical Physics and Materials Science, HUN-REN Centre for Energy Research, Konkoly Thege M. út 29-33, Budapest H-1121, Hungary
[c] Department of Materials Science, Montanuniversität Leoben, Franz-Josef-Strasse 18, A-8700 Leoben, Austria

ARTICLE INFO

Keywords:
X_2BC
Sputter deposition
Ab initio calculations
Elastic properties

ABSTRACT

This article presents theoretical and experimental findings on the stability of orthorhombic $(Mo_{1-x}Nb_x)_2BC$ phase in magnetron sputtered coatings, where molybdenum is gradually replaced by niobium. Magnetron co-sputtering of Mo_2BC and Nb_2BC targets was used to best preserve the metal/non-metal ratio of 1/1. The theoretical calculations were based on replacing Mo atoms in orthorhombic Mo_2BC cell, thus creating a $(Mo_{1-x}Nb_x)_2BC$ solid solution. It is predicted to be stable up to 37.5% of Mo atoms replaced by Nb, at which point also the elastic modulus and the shear modulus are the highest. Simultaneously, the enthalpy of formation of this material suggests that it should be more stable than, e.g. the commonly used and studied TiAlN. Experiments have confirmed that orthorhombic $(Mo_{1-x}Nb_x)_2BC$ does not form at high Nb contents, and fcc NbC-like structure was observed instead. All coatings were shown to be columnar with grains in the nanometre range with amorphous regions between the columns. This led to reduced stability of the orthorhombic Mo_2BC-like phase compared to the theoretical calculations. At the limit of the stability of the orthorhombic cell, the hardness of the coating was enhanced by 25% and the elastic modulus by 60%. *Ab initio* calculations indicate that lattice strain is responsible for the mechanical properties' enhancement.

1. Introduction

Investigation of ternary boron-carbides in bulk form has been ongoing for many decades since the 1950s. Many systems have been investigated, and one of them was found to crystallize in an orthorhombic cell with an X_2BC stoichiometry – Mo_2BC [1–4]. An exhaustive list of other investigated systems, none exhibiting the same X_2BC phase, can be found in the supplementary material.

Ideas about the concepts of using ternary boron carbide coatings as hard coatings were thoroughly discussed in 1986 [5]. It has been argued that, generally, another set of parameters – the fabrication or deposition parameters – needs to be taken into account for coatings in contrast to the fabrication of bulk materials. The idea of using multilayer or multiphase coatings was proposed. Among others, coatings from the Ti–B–C, either in the form of a (nano)composite or as multilayered systems, were hypothesized to be good candidates for experimental research. The multilayer concept was further yet still predominantly theoretically refined [6]. The relations between constitution, microstructure, properties and application behaviour developed for bulk materials were used to describe the behaviour of layered materials and the parallels between bulks and coatings were drawn. Experimental measurements of the wear of TiC–TiB_2 multilayers were presented, documenting the possibilities of the practical use of materials presented in the previous decade. Coatings belonging to the Ti–B–C system were prepared by reactive magnetron sputtering of TiB_2 target in an Ar–C_3H_8 atmosphere [7].

But the multilayering principle can be brought down to the fundamental level. This points us to Mo_2BC first described in bulk form in 1963 [1]. This material in the form of a thin film was re-discovered in 2009 when it was calculated that owing to its structure similar to the MAX phases with altering planes containing stiff carbidic and boridic bonds with a high degree of ionicity and weaker metallic planes, this material should exhibit a very rare combination of high stiffness and hardness together with ductility and fracture resistance [8]. Since then, crystalline Mo_2BC coatings were prepared by DC [8–10], pulsed-DC magnetron sputtering [11] as well as High Power Impulse Magnetron Sputtering (HiPIMS) [12]. Apart from Mo_2BC, a whole family of similar X_2BC materials with X = Ti, V, Zr, Nb, Hf, Ta and W with the rare combination of stiffness and ductility was theoretically proposed by

* Corresponding author.
E-mail address: jzenisek@mail.muni.cz (J. Ženíšek).

https://doi.org/10.1016/j.actamat.2024.119741
Received 31 October 2023; Received in revised form 2 February 2024; Accepted 6 February 2024
Available online 10 February 2024

ab initio simulations [13]. However, none of these crystalline X_2BC coatings have been reliably and unambiguously prepared so far, despite many of the systems such as W–B–C [14–17], Nb–B–C [18–20] and Ta–B–C [21] being extensively studied.

In this work, we will study the effect of the substitution Mo by Nb in the Mo_2BC coating on the structure and properties of the $(Mo_{1-x}Nb_x)_2BC$ system. Niobium is a neighbour of Mo in the periodic table of elements with almost the same size and crystallizes as a metal in the same lattice as metallic Mo. The Nb_2BC phase has even lower formation enthalpy than Mo_2BC [13], and its formation is thermodynamically more favourable compared to the formation of binary NbB and NbC phases [20]. However, the orthorhombic crystalline Mo_2BC phase has been experimentally prepared, while Nb_2BC was not. Nb was chosen as it should also form the crystalline orthorhombic Nb_2BC phase, and Mo_2BC is used to serve as a stabilizing "scaffolding" for the orthorhombic Nb_2BC phase. We theoretically as well as experimentally systematically replace molybdenum in Mo_2BC with niobium in the whole composition range from Mo_2BC to Nb_2BC while preserving the $(Mo_{1-x}Nb_x)_2BC$ chemical stoichiometry as much as possible. We describe the effects of the niobium content on the microstructure and the crystalline structure and their links to the mechanical properties of $(Mo_{1-x}Nb_x)_2BC$ thin films.

2. Materials and methods

2.1. Ab initio calculations

Mechanical properties of $(Mo_{1-x}Nb_x)_2BC$ solid solutions were calculated using the density functional theory [22,23] as implemented in the Quantum ESPRESSO package [24,25]. 3 × 1 × 3 supercells consisting of 144 atoms based on the orthorhombic (*Cmcm*, spacegroup #63) Mo_2BC structures were prepared with the special quasi-random structure method [26,27] and were fully relaxed with respect to the cell shape and atomic positions. A plane-wave pseudopotential method with PBEsol pseudopotentials from the SSSP precision database (version 1.1.2) [28–32], PBEsol exchange–correlation potential [33], plane-wave cut-off energy of 55 Ry and k-point grid of 4 × 2 × 4 were used for the calculations. Elastic properties were calculated with the stress–strain method [34] and the polycrystalline bulk (B), elastic (E) and shear (G) moduli, as well as Poisson's ratio (ν), were obtained within the Hill's approximation [35,36]. The effective elastic modulus for comparison with nanoindentation measurements was calculated as $E_{\mathrm{ef}} = E/(1-\nu^2)$. Integrated crystal orbital Hamilton populations (ICOHP) analysis was performed using the LOBSTER package [37,38]. All computational results with further details are available in the NOMAD archive [39–41].

2.2. Deposition

The Mo_2BC, Nb_2BC and $(Mo_{1-x}Nb_x)_2BC$ coatings were deposited in a high-vacuum system using non-reactive magnetron sputtering of Mo_2BC and Nb_2BC targets (Sindlhauser, 99.5%, 3″ diameter). Before the deposition, silicon substrates (10 mm × 45 mm strips with (100) orientation) were cleaned in an ultrasonic bath for 3 min in isopropanol and, after drying, subsequently mounted on a heater installed inside the vacuum chamber of the magnetron sputtering device. The Mo_2BC and Nb_2BC targets were positioned in a confocal configuration approximately 10 cm above the Si strip and along the longitudinal axis of the strip so that the axes of the targets pointed at the centre of the strip (as schematically shown in Fig. 1).

Such arrangement leads to the formation of $(Mo_{1-x}Nb_x)_2BC$ coatings with gradual change of the Mo/Nb ratio along the specimen. The base pressure before depositions was ~0.1 mPa, and the working pressure was 0.2 Pa of Ar (99.99%). Before depositions, the substrates were heated to 750 °C, and that temperature was held during the depositions to promote the crystallinity of the coatings. The targets

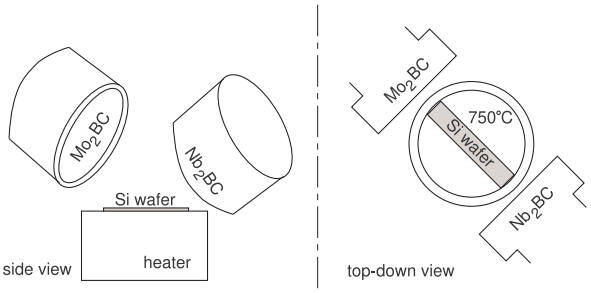

Fig. 1. The arrangement of targets and substrate for deposition with gradient compositions.

were powered by DC power supplies. The combinations of powers on Mo_2BC/Nb_2BC targets, respectively, were the following: 250 W/0 W, 250 W/50 W, 250 W/100 W, 250 W/150 W, 250 W/200 W, 0 W/200 W. The first and the last power settings formed pure Mo_2BC and Nb_2BC coatings, respectively. Before the start of each deposition, the Si substrate was shuttered off, and the power on both targets was gradually increased (+5 W/min) to the desired level. After ramping up to full power, the targets were cleaned for 10 min. Depositions started afterwards by removing the shutter from the specimen position. Each deposition took 60 min and was finished by placing the shutter back above the specimen. The deposited specimen was left in the deposition chamber overnight to cool down under vacuum conditions.

2.3. Analyses

Oxford Instruments X-MAX 50 Energy-Dispersive X-ray Spectrometer coupled to a Tescan Mira 3 scanning electron microscope was used to determine the composition of the prepared samples. The quantification was done after calibration with Mo_2BC and Nb_2BC sputtered references with 8 kV electron accelerating voltage. However, it needs to be kept in mind that the simultaneous quantification of very light B and C together with heavier Mo and Nb can lead to larger uncertainties. Therefore, during later discussion, we focus more on the trends rather than the specific values of the composition. Further details about the quantification procedure are given in the Supplementary material. In addition to deposited elements (Mo, Nb, B, C), up to 10 at.% of O and ~1 at.% of Ar were detected in the deposited coatings.

X-ray diffraction analysis (XRD) was used to investigate the crystallinity of the deposited $(Mo_{1-x}Nb_x)_2BC$ coatings. The instrument used for this analysis was Rigaku Smartlab diffractometer with a Cu K_α radiation source. All measurements were performed in the Bragg–Brentano configuration. Lamellae for TEM investigation were extracted from the deposited coatings by focused ion beam technique (FIB) with a Thermo Scientific Scios 2 Dual Beam equipment. The final steps in FIB preparation were made at 2 kV. The TEM investigations were performed in a C_s corrected 200 kV Themis (Thermo Fischer) microscope. Selected Area Electron Diffraction (SAED) patterns were calibrated with Si substrate reflections and evaluated using Process Diffraction software [42].

The mechanical properties of the deposited coatings were evaluated using a Hysitron TI980 nanoindenter equipped with a Berkovich-type diamond tip with a diameter of ~50 nm. The indenter tip calibration was performed on a certified fused silica sample (Bruker). In order to find the critical indentation depths where the substrate influence starts, standard quasistatic nanoindentation tests with 20 unloading segments were carried out in a load-controlled regime with a constant loading rate of 0.2 mN/s. From the evaluation of the unloading segments' depth profiles, the hardness and elastic modulus data were obtained. The proper maximum loads used for further measurements were chosen according to the obtained depth profiles. The main measurements

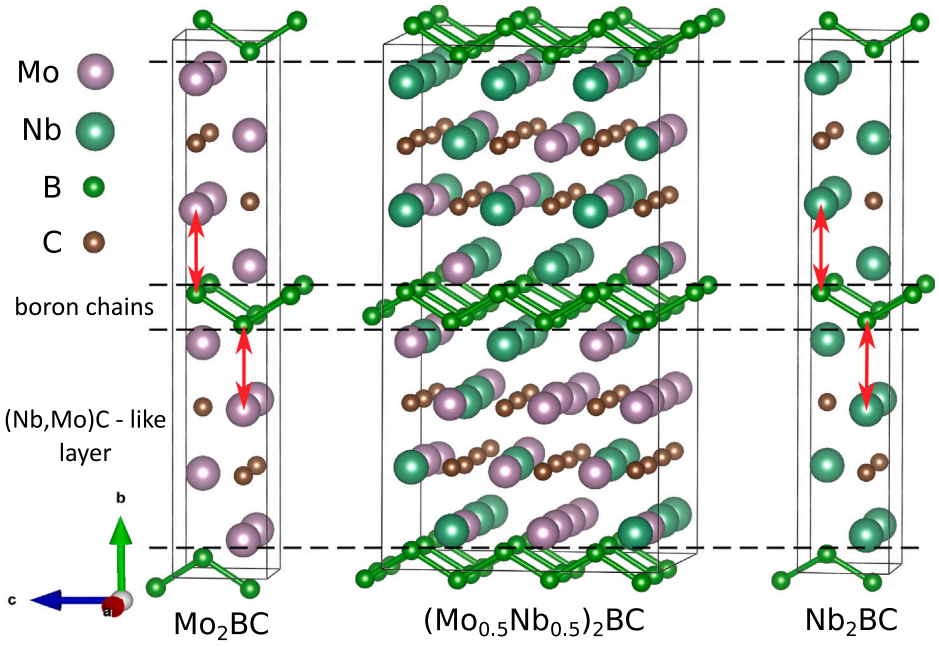

Fig. 2. Atomic structures of Mo_2BC, $(Mo_{0.5}Nb_{0.5})_2BC$ and Nb_2BC. Boron-boron bonds and dashed lines highlight the nano-laminated structure of the cell, consisting of alternating layers of boron chains and (Mo,Nb)C-like layers. Red arrows mark the second nearest metal neighbours of the B atoms, which will be further discussed below. Visualized with VESTA [44].

were done utilizing rapid mechanical property mapping (XPM) using a constant loading rate of 100 mN/s. Each measured point on the specimen was calculated as an average of at least 100 indentations (matrix 10 × 10, distance between individual indentations 4 μm). Three different points were chosen on each specimen and at every composition to carry out the mechanical property maps. The standard Oliver and Pharr model [43] was used to evaluate the mechanical properties. The effective elastic modulus E_{ef} defined as $E_{ef} = \frac{E}{1-\nu^2}$, where E and ν are the Young's modulus and the Poisson's ratio of the coating, is used for the expression of the elastic properties of the coatings, as it carries only the information of the sample as opposed to the reduced elastic modulus that combines the properties of the measured coating and the indenter.

3. Results and discussion

3.1. Ab initio modelling

Previous experiments have shown that Mo_2BC can be prepared experimentally in thin films [8,9,11,12]. Theoretical calculations have shown that the formation enthalpy of Nb_2BC is lower than of Mo_2BC [13] and detailed analysis of the enthalpy of formation per atom of the ternary Nb_2BC showed that it is lower than the formation enthalpy of NbB + NbC binary phases [20]. These theoretical results suggest that it is easier to prepare the orthorhombic Nb_2BC phase than the orthorhombic Mo_2BC phase. Let us, therefore, study what happens as Mo in the crystalline Mo_2BC lattice is substituted by Nb. Images of the Mo_2BC, Nb_2BC and mixed solid solution are shown in Fig. 2. *Ab initio* calculations of the elastic properties of the crystalline orthorhombic Mo_2BC, $(Mo_{1-x}Nb_x)_2BC$ solid solutions and Nb_2BC shown in Fig. 3 exhibit non-linear trends of the elastic properties with respect to the Nb/(Mo+Nb) ratio x in the $(Mo_{1-x}Nb_x)_2BC$ notation. When Nb is added to Mo_2BC, it initially leads to an increase of the elastic and shear moduli, with the maximum value of 521 GPa and 211 GPa at $x = 0.25$ for elastic and shear modulus, respectively, an increase of 7% and 9% as compared to the values of 487 GPa and 193 GPa for Mo_2BC. Further increase of Nb concentration leads to a significant decrease of both elastic and shear moduli to values of 450 GPa and 182 GPa at $x = 0.5$,

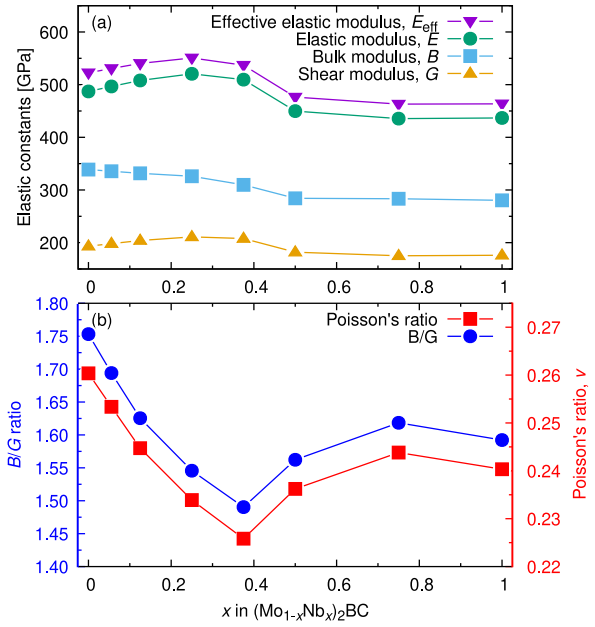

Fig. 3. (a) Elastic, effective elastic, bulk, and shear moduli, (b) bulk over shear modulus ratio and Poisson's ratio as a function of the x = Nb/(Mo+Nb) ratio.

and the values stay mostly constant or decrease slightly in the rest of the composition range when further Nb is added, with calculated values of 436 GPa and 176 GPa for elastic and shear modulus for Nb_2BC. Bulk modulus does not exhibit this local maximum and decreases over the whole compositional range, with most of the decrease happening between Mo_2BC, with value of 339 GPa, and $x = 0.5$ with value of 284 GPa. Both the B/G ratio and Poisson's ratio show a minimum at $x = 0.375$, with values of 1.49 and 0.226, respectively, as compared to values of $B/G = 1.75$, $\nu = 0.26$ for Mo_2BC and $B/G = 1.59$, $\nu = 0.24$ for Nb_2BC (see Fig. 3). This suggests that the mixed $(Mo_{1-x}Nb_x)_2BC$

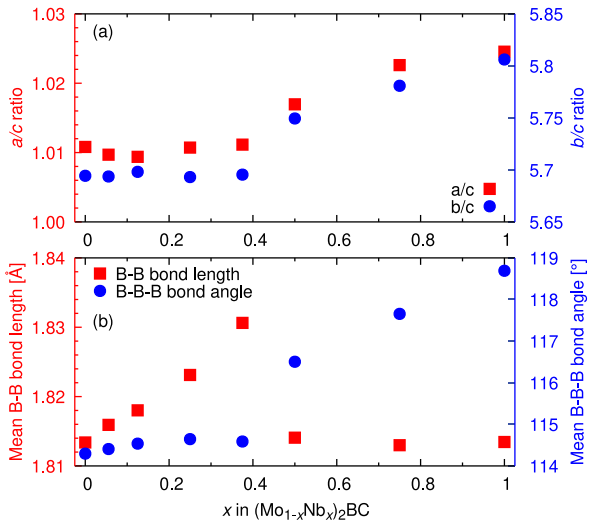

Fig. 4. (a) a/c and b/c lattice parameter ratios, (b) mean B–B bond length and mean B–B–B bond angle.

material has inferior ductility to Mo_2BC in the whole composition range.

The non-linear trends of the elastic properties can be rationalized based on the evolution of the geometry of the lattice. As the Nb content increases and while the Nb/(Mo+Nb) ratio $x \lesssim 0.375$, the cell expands homogeneously as based on the ratios of the lattice parameters (Fig. 4(a)), the B–B bonds are elongated (Fig. 4(b)), and are more strained as can be seen from the less negative integrated crystal orbital Hamilton population (ICOHP) shown in Fig. 5(a), where negative ICOHP can be loosely interpreted as bond strength [45]. Additionally, the B–B–B bond angles increase only marginally for x up to 0.375, while there is a steep decrease for larger Nb concentrations. Therefore, between $x = 0.375$ and $x = 0.5$, the structure deforms significantly, and the B–B zigzag chains start to straighten, returning the B–B bond length closer to their value in Mo_2BC and release of the stress. The linking between the boron chains and the metal-carbon layers is significantly weakened, as can be seen in Fig. 5(b) and (c) from the changes in the ICOHP between the boron and both its first and second metal nearest neighbours. The average ICOHP between the metal atoms decreases slightly when more Nb is added, and the C-metal average ICOHP shows a similar trend to the boron (Fig. 5(d) and (e)). However, in general, the magnitude of the differences is smaller than what can be observed for the boron-boron and boron-metal bonds ICOHP. The behaviour of the boron chains was already shown to be the main factor behind the Mo_2BC ductility [46], and here we highlight the similar crucial role of the boron chains also in the mechanical properties of $(Mo_{1-x}Nb_x)_2BC$.

Therefore, as Nb is added into the Mo_2BC structure, replacing Mo, the larger Nb radius leads to an increase in volume and the lattice parameters. Due to the material's nanolaminated-like structure, which can be understood as stacked metal-terminated slabs of fcc (Mo,Nb)C with the metal atoms connecting to layers of boron zigzag chains, where Nb is incorporated only into the former, it leads to increased tensile stress within the boron zigzag chains and additionally compressive stress within the carbide-like layers. This is based on the difference of average Nb–C and Mo–C bond length in the slab plane in the $(Mo_{1-x}Nb_x)_2BC$ structure, e.g., 2.18 Å at $x = 0.25$, and Mo–C and Nb–C bond lengths of 2.19 Å and 2.25 Å in NaCl-type MoC and NbC, respectively, based on Materials Project (mp-910, mp-2746) [47]. The Mo_2BC structure can accommodate the internal stress only up to $x \lesssim 0.375$ while homogeneously expanding. In this region, the incorporation of the niobium leads to an increase in the elastic and shear moduli. As yet more niobium is introduced into the cell, which the structure cannot

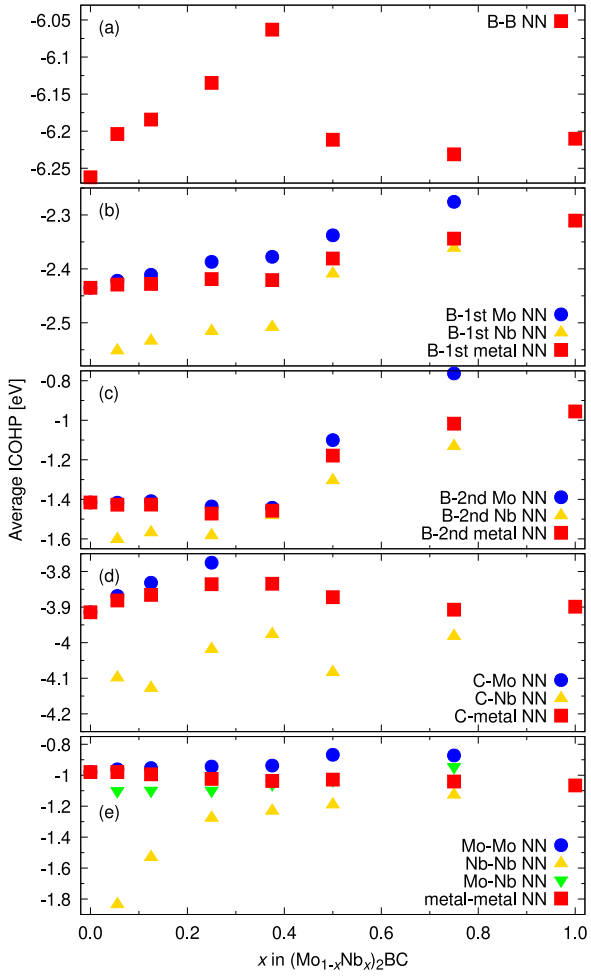

Fig. 5. Average values of the ICOHP for (a) B–B, (b) B-metal nearest neighbours (NN), (c) B-metal second nearest neighbour, (d) C-metal, (e) metal–metal bonds.

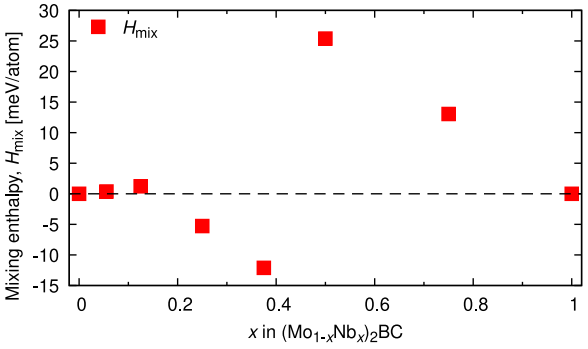

Fig. 6. Mixing enthapy, H_{mix}, as calculated from the energy difference of the solid solutions and the pure Mo_2BC and Nb_2BC phases.

further accommodate, the Mo_2BC structure destabilizes and starts to deform significantly. This leads to weakened crosslinking between the boron chains and the carbide-like layers and to a decrease in elastic constants.

Let us now look at the thermodynamical stability of the $(Mo_{1-x}Nb_x)_2BC$. The mixing enthalpy of the $(Mo_{1-x}Nb_x)_2BC$ is shown in Fig. 6 and indicates the stability of the solid solution with respect to the ternary Mo_2BC and Nb_2BC phases. It is slightly positive for the low Nb contents with the value of ~1 meV/atom at $x = 0.125$. However, it

goes negative down to –12 meV/atom at $x = 0.375$. The changes of the structure between $x = 0.375$ and $x = 0.5$, as discussed in the previous section, also correspond to an increase of the mixing enthalpy by almost 40 meV/atom to positive values, suggesting metastability of the solid solution. However, the maximum value is still below 30 meV/atom, i.e., 3 times lower than that, for example, TiAlN, which is known to decompose spinodally [48], but also to be routinely synthesized by PVD as a metastable solid solution. The negative mixing enthalpy highlights that if the solid solution could be successfully prepared, it should have reasonable stability concerning decomposition into the ternary Mo_2BC and Nb_2BC better than e.g. TiAlN, at least in the compositions range of Mo/(Mo+Nb) ratios $x \lesssim 0.375$.

3.2. Chemical profiles of $(Mo_{1-x}Nb_x)_2BC$ coatings with varying x

In order to verify the theoretical predictions, four $(Mo_{1-x}Nb_x)_2BC$ coatings with gradually evolving Mo/Nb ratios were produced by combinatorial magnetron co-sputtering with four combinations of plasma discharge powers on the Mo_2BC and Nb_2BC targets. Ar and O were measured as expected impurities. The concentration of O increases from about 5 at.% in the Mo-rich end to nearly 10 at.% in the Nb-rich side of the specimens. The concentration of Ar remained below 1 at.% in all specimens at all measured positions. The obtained x ratios as dependencies on the position on the samples are plotted in Fig. 7. The four deposited samples cover the Nb/(Mo + Nb) ratios of ~0.04–0.65, where each composition can be found on at least one sample. The deposition conditions (i.e. low pressure and low substrate-target distance) were chosen to preserve the $(Mo_{1-x}Nb_x)_2BC$ stoichiometry as well as possible. The B/C ratio of the light non-metallic elements and the (Mo+Nb)/(B+C) ratio showing the metal/nonmetal ratio for all the deposited samples are plotted in Figure S4 in the supplementary material. A detailed plot of the chemical composition of the samples can be seen in the supplementary material in Figure S5. The B/C ratios are nearly constant over the length of each sample and are ~0.6 for samples prepared with 50, 100 and 150 W on the Nb_2BC target and ~0.5 for the sample prepared with 200 W on the Nb_2BC target. As the B/C ratio is less than one, the measurements indicate partial loss of boron. This may be at least partially due to measurement artefacts, as EDX ordinarily overestimates carbon content to up to 5–10 at.%, which cannot be fully mitigated even by standard-based quantification. Some boron may have been lost in the transport due to its higher scattering on background gas atoms, as boron is the lightest element. However, carbon is not much heavier, and a similar degree of scattering can be expected [49]. The (Mo+Nb)/(B+C) ratio is again nearly constant in any place of any sample, corresponding to approximately $(Mo_{1-x}Nb_x)_{1.6}BC$. This value would indicate a deficit of metals in the sample. Due to dominantly line of sight sputtering with little scattering, this is improbable, and the metal value is likely underestimated by the measurement method.

3.3. Microstructure

First, XRD analysis allows us to compare regions of the same composition on different samples deposited with different combinations of powers on the Mo_2BC and NB_2BC targets to verify that the crystalline structure depends only on the composition. For example, the region with $x = 0.09$ can be found in samples deposited with powers on Mo_2BC/Nb_2BC targets of 250 W/50 W as well as with 250 W/100 W. In the latter case, that region is shifted closer to the Mo-rich end of the specimen. We crosschecked five such areas on different samples. An example of the comparison of the XRD patterns for $x = 0.30$ on samples prepared with powers of 100 W and 150 W on the Nb_2BC target is shown in the supplementary material in Figure S6. Both samples show the same broad double peak between 30° and 50° and small wide peaks around 58° and 72°. In general, regions with the same composition always exhibited the same type of diffraction patterns, and we can conclude that the deposition parameters were always similar enough that the crystalline structure depends only on the chemical composition.

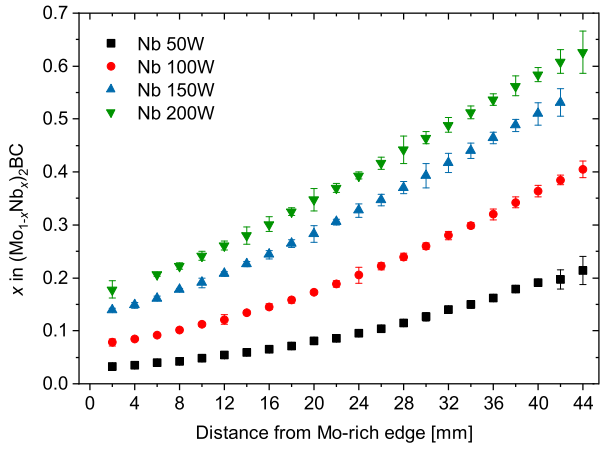

Fig. 7. The x = Nb/(Mo+Nb) ratios measured by EDX for different powers on the Nb_2BC target and constant power of 250 W on the Mo_2BC target.

Now, we can study the evolution of the crystalline structure of the $(Mo_{1-x}Nb_x)_2BC$ coatings as molybdenum is gradually replaced by niobium. Fig. 8 shows the X-ray diffraction patterns of the deposited Mo_2BC, selected $(Mo_{1-x}Nb_x)_2BC$, and Nb_2BC coatings. The XRD profiles on the top and on the bottom in Fig. 8 are for structures corresponding to the ternary Mo_2BC and Nb_2BC systems, respectively. The XRD patterns between those correspond to quaternary $(Mo_{1-x}Nb_x)_2BC$ coatings with Nb content increasing from the top to the bottom. The patterns of the $(Mo_{1-x}Nb_x)_2BC$ coatings are denoted by their x = Nb/(Mo+Nb) ratios. Samples with the x ratios of 0.05, 0.09, 0.12, 0.17, 0.25, 0.33, 0.5 and 0.67 are selected to show the evolution of the XRD patterns. The diffractogram of the pure Mo_2BC ($x = 0$) coating exhibits reflections typical for the orthorhombic lattice in the *Cmcm* (#63) space group (COD 00-029-0913). These are namely the peak at 29.3° corresponding to the (110) reflection with the measured d-spacing of 3.016 Å, the wide region from 30° to 50° containing several reflections with the most prominent being (130) with the reference d-spacing of 2.723 Å at 32.8°, (041) with reference $d = 2.493$ Å at 36.1°, (150) with reference $d = 2.306$ Å at 38.9° and (080) with reference $d = 2.169$ Å together with (111) with reference $d = 2.151$ Å close to each other at ~41.5°, the peak at 60° corresponding to the (200) reflection with reference $d = 1.543$ Å and a very broad peak from 61° to 80° again composed of many less intensive reflections. The diffractogram of the pure Nb_2BC ($x = 1$) sample can be indexed by peaks of fcc NbC in the $Fm\bar{3}m$ (#225) space group (PDF 00-038-1364). The peak at 34.3° corresponds to the (111) reflection with the measured d-spacing of 2.608 Å, the one at 40.7° to the (200) reflection and measured d-spacing 2.219 Å, the peak at 58.7° to (220) with measured $d = 1.571$ Å, at 69.3° to (311) with measured $d = 1.357$ Å, 73.3° to (222) with measured $d = 1.281$ Å, a small peak at 87.2° to (400) with measured $d = 1.116$ Å and at 98° to (331) with measured $d = 1.020$ Å. XRD patterns for $(Mo_{1-x}Nb_x)_2BC$ samples with low Nb content are similar to the profile for Mo_2BC, and the patterns, where Nb dominates over Mo, tend to be similar to the pattern for Nb_2BC. This is most clear in the region of the main diffractions between 30° and 50°. As Nb is gradually added into the $(Mo_{1-x}Nb_x)_2BC$, the peak at ~36° corresponding to the (041) reflection in Mo_2BC is getting more pronounced and is shifting to lower angles transforming into (111) peak of fcc NbC. At the same time, the peak at ~41.5° corresponding to the (080) and (111) reflections of Mo_2BC is gradually diminishing while not changing its position. At the x of 0.33 the (200) peak of NbC becomes noticeable and gets more prominent as more Nb is added into the coating. While all samples exhibit only very

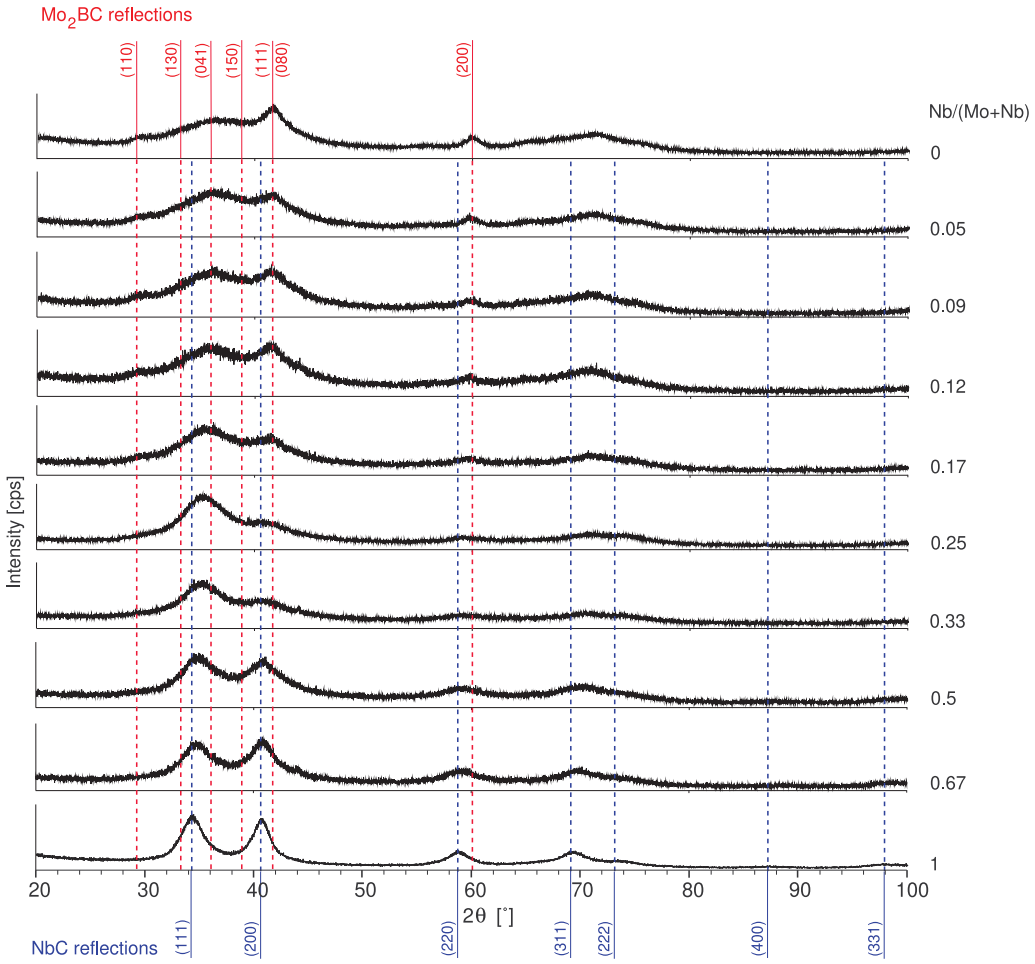

Fig. 8. X-ray diffractograms of the coatings. Positions of selected reflection from the Mo_2BC cell are shown by red lines together with their Miller indices on top of the figure. Positions of NbC are highlighted by blue vertical lines with their Miller indices on the bottom of the figure.

wide peaks suggesting nanocomposite crystallites with size <5 nm, the samples with the x of 0.17–0.33 show the least defined peak at ~40°, while the FWHM of the peak at ~36° does not significantly change. This means that these are the closest to an amorphous or a short-range ordered structure. Probably, conditions least favourable for crystallite growth, such as competitive growth between the observed phases are taking place here. Coatings with the Nb/(Mo + Nb) ratio <0.25 exhibit dominant orthorhombic Mo_2BC structure, while those with Nb/(Mo + Nb) ratio >0.25 exhibit predominantly the fcc NbC structure.

Microstructures of Mo_2BC, $(Mo_{1-x}Nb_x)_2BC$ with $x = 0.25$, and Nb_2BC were further investigated by TEM. The overview TEM images complemented with the corresponding SAED patterns are shown in Fig. 9. All the coatings have a tilted columnar structure where amorphous column walls separate the columns. The SAED rings of Nb_2BC coating can be indexed as an fcc structure with the lattice parameter of 4.43 Å. This lattice parameter is somewhat smaller than the values of 4.426–4.447 Å reported for NbC [50], possibly due to the incorporation of boron, vacancies or stress in the coating. Its structure is random nanocrystalline. Mo_2BC coating can be better indexed as textured orthorhombic. The strong reflections of the orthorhombic structure coincide with the fcc structure, and its weak reflections coincide with cubic reflections forbidden in the fcc system. This is illustrated by indexing of the SAED rings according to fcc and according to orthorhombic cell, as is more discussed in the Addendum. This coincidence in the diffraction positions also indicates the strong relation of the orthorhombic structure of Mo_2BC to the cubic one — as discussed previously, the orthorhombic structure is composed of planes of metal terminated fcc carbide linked by the boron chains. Considering the strong reflections and applying the fcc notation, the texture can be interpreted as an fcc 111 texture. The direction of the preferential orientation is between the surface normal and the direction of the columns. The $(Mo_{1-x}Nb_x)_2BC$ with $x = 0.25$ shows the best match with the fcc structure. The sample is 111 textured as well, and the direction of the preferential orientation is between the surface normal and the direction of columns. The fcc cell exhibits the lattice parameter of 4.375 Å, smaller than that of the Nb_2BC sample. At the same time, this sample has the broadest SAED rings (and also XRD peaks). This again points to the composition, where the development of a single crystalline phase is the most limited.

The column width and grain sizes of the deposited coatings can be judged from the high-resolution images in Fig. 10. In the Mo_2BC sample, the column width is ~10 nm, and the columns are interrupted by planar defects perpendicular to the columns. The density of planar defects, defining the grain size, is in nm range which is the reason of the broadening of (111) reflections. In the Nb_2BC sample, the column width is ~3 nm. The grains span the whole width of the columns and are elongated in the column growth direction up to ~15 nm. The structure of $(Mo_{1-x}Nb_x)_2BC$ with $x = 0.25$ is a combination of those for Nb_2BC

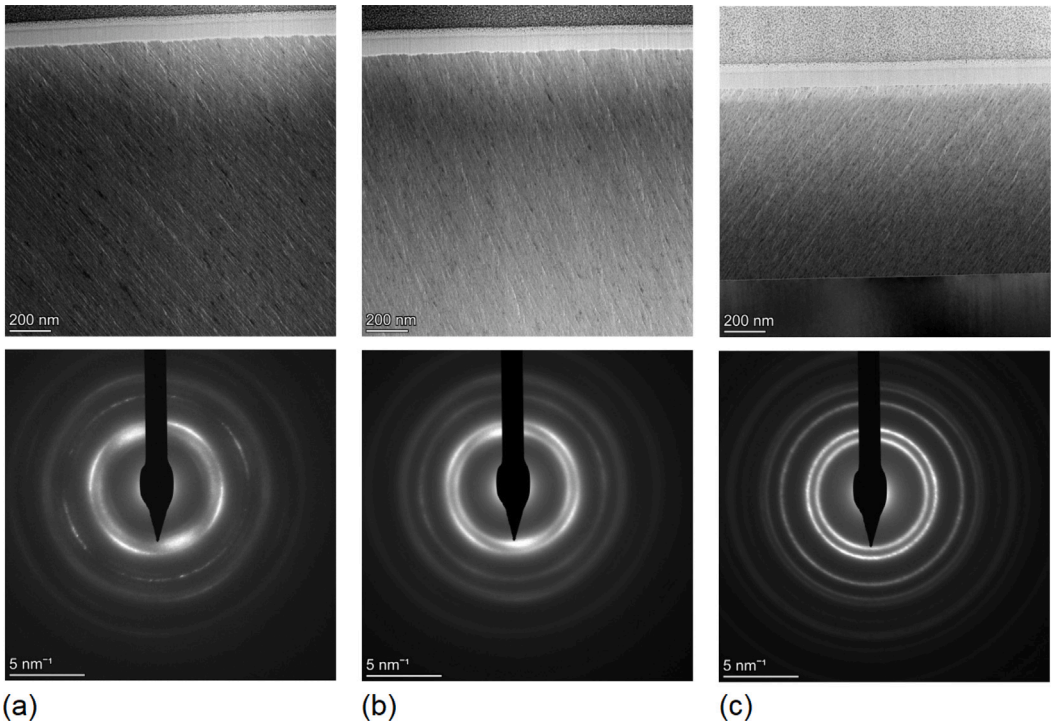

Fig. 9. Bright field overview images of deposited materials together with SAED diffraction patterns for Mo_2BC (a), $(Mo_{1-x}Nb_x)_2BC$ with $x = 0.25$ (b), and Nb_2BC (c).

and Mo_2BC. It can be judged from the HR image in Fig. 10 that there are regions with small (<3 nm) grains and also columnar regions with planar defects and larger grains up to ~10 nm.

Elemental maps of Mo, Nb, and O in the deposited coatings measured by STEM-EDX are shown in Fig. 11. In Mo_2BC (a), the Mo content is a little lower in the column walls while the O content is slightly increased there. Similarly, in Nb_2BC (c), the column walls are poor in Nb and considerably enriched in O. In the case of $(Mo_{1-x}Nb_x)_2BC$ with $x = 0.25$ (b), Mo-rich and Nb-rich regions can be observed in the MoNb map, and the column walls show a slightly increased O content.

In summary, the Mo_2BC coating had an orthorhombic structure, as was used for the calculations. Unlike the calculations, the sample exhibited a nanocrystalline multiphase structure regarding the composition as well as the crystalline structure. Despite Nb_2BC having an even lower formation enthalpy than Mo_2BC, it did not form, and an fcc phase that has a similar lattice parameter to NbC formed instead. The $x = 0.25$ sample exhibited the smallest grain size and the fcc structure.

Let us compare the theoretical and the experimental results. The orthorhombic $(Mo_{1-x}Nb_x)_2BC$ was predicted to have negative mixing enthalpy when replacing molybdenum with niobium up to the x of ~0.375, as was seen in Fig. 6. Experimentally, the orthorhombic Mo_2BC-like phase was stable only to the x ratio of ~0.25, where the growth of an fcc phase was evidenced by TEM and by the x ratio of ~0.33, this was also clearly seen on XRD patterns plotted in Fig. 8. The formation of the orthorhombic Mo_2BC-like phase happened up to a somewhat lower Nb content than suggested by the calculations. This is partly due to the nanocomposite structure of the Mo_2BC sample compared to the fully crystalline calculations. Another reason is that in the experiments, the predicted orthorhombic Nb_2BC phase used in the calculations was not formed. This is despite the formation of orthorhombic Nb_2BC being thermodynamically more favourable than the formation of cubic NbC and orthorhombic NbB, as was shown by the calculation of the formation enthalpies of the ternary Nb_2BC and comparison of the sum of the respective NbB and NbC binaries [20]. However, the lack of formation of Nb_2BC is consistent with the literature [18,20]. Even heating stoichiometric NbC and NbB powders to 1500 °C did not result in the formation of Nb_2BC, showing a considerable thermodynamic barrier for such process [20]. Our calculations, therefore, describe the physical situation very well until approximately 1 of 4 molybdenum atoms is replaced by niobium. Then, the correspondence to the experiments is increasingly limited as the orthorhombic Mo_2BC-like phase becomes unstable, the grain size significantly decreases, and the grain boundaries can start to have a strong impact, and, finally, the fcc NbC-like phase forms.

3.4. Elasticity and hardness

The indentation hardness and the effective elastic modulus for all the samples were evaluated from three nanoindentation measurements for each selected x ratios are plotted in Fig. 12. The effective elastic modulus E_{ef} for pure Mo_2BC is approximately 240 GPa, and it increases until the x of 0.25 when E_{ef} reaches the highest value of ~380 GPa. Further increase of Nb in $(Mo,Nb)_2C$ decreases the E_{ef} until 185 GPa is reached for pure Nb_2BC. The indentation hardness H_{it} for pure Mo_2BC is 19 GPa and increases after formation of $(Mo_{1-x}Nb_x)_2BC$ mixture up to 23 GPa for x of 0.25. Further increase of Nb in $(Mo_{1-x}Nb_x)_2BC$ decreases the H_{it} down to 18.5 GPa for the case of pure Nb_2BC. The maximum in both the E_{ef} and the H_{it} corresponds to the transition region between the orthorhombic Mo_2BC-like and fcc NbC-like profiles, which occurs near the x ratio of 0.25, as was seen in the XRD diffractograms and TEM. The measured values of the hardness are on par or below those reported in the literature for NbC [51,52] and Nb–B–C [18], probably due to the small grain size resulting in an inverse Hall-Petch effect [53], columnar structure and amorphous regions in the coatings at the column walls.

Let us compare the theoretically calculated effective modulus plotted in Fig. 3 and the measured values plotted in Fig. 12. The predicted trends, i.e. a gradual increase of the effective modulus when niobium is

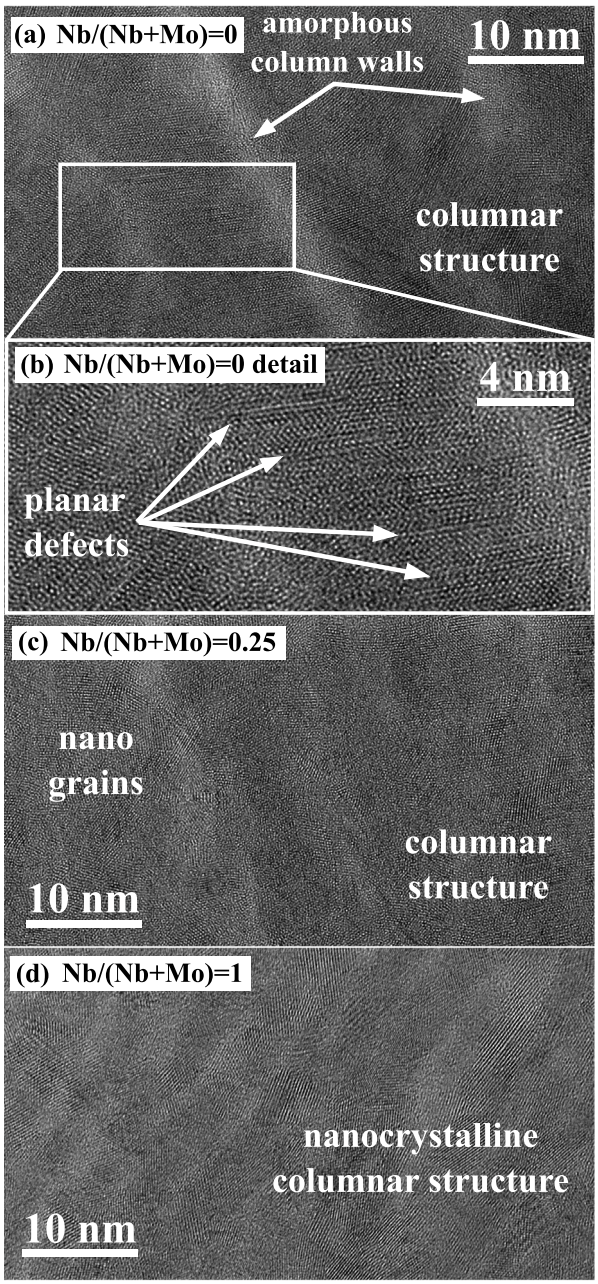

Fig. 10. Comparison of HR-TEM images of (a) Mo_2BC, (b) detail of the observed planar defects in Mo_2BC, (c) $(Mo_{1-x}Nb_x)_2BC$ with $x = 0.25$, (d) Nb_2BC.

added up to one atom per four molybdenum atoms being substituted by niobium, followed by a decrease, are accurately reproduced in the experiments. Trends above the x ratio of ~0.3 are affected by the fact that Nb-rich coatings did not form the Nb_2BC phase, but they formed the fcc NbC-like phase instead. Therefore, a much steeper decrease in the effective modulus was measured compared to the calculations. Moreover, the absolute values of the calculated effective elastic modulus are much higher than the experimentally measured ones. This is due to the small grain sizes of the coatings. Value of (460±21) GPa was previously reported for the elastic modulus of Mo_2BC films with better crystallinity [8], which is in agreement with the value of 487 GPa predicted in this work. However, the trends correspond to the theoretical predictions, suggesting that while the presence of high quality Mo_2BC-like orthorhombic phase is crucial to achieving the high elastic modulus, there are similar mechanisms behind the non-linear behaviour even in very small grains and the mechanical properties are enhanced due to lattice strain induced by molybdenum substitution by niobium.

The ratio of the hardness to the effective elastic modulus H/E has been shown to point to the fracture toughness of a material, whereby a larger H/E ratio is correlated with better fracture resistance and increased ductility of a material [54,55]. The resistance to plastic deformation and wear behaviour of a material are often considered to depend on the H^3/E^2 ratio [55,56]. These are plotted in Fig. 13. Both decrease as Nb is added to $(Mo_xNb_{1-x})_2BC$ with the exception of pure Nb_2BC with the most pronounced crystalline NbC phase and the superfluous boron and niobium forming probably amorphous tissue phase. The worsening of the mechanical properties with increased niobium content was also predicted by the *ab initio* calculations shown in Fig. 3. The discrepancy between the B/G ratio evolution and the experimentally observed H/E and H^3/E^2 ratios for $(Mo_xNb_{1-x})_2BC$ coatings with $x \gtrsim 0.4$ can be ascribed by the orthorhombic structure being calculated, while the cubic lattice and tissue phase being formed instead.

4. Conclusion

The stability and the mechanical properties of $(Mo_{1-x}Nb_x)_2BC$ solid solutions were calculated *ab initio*. The non-linear behaviour of the elastic properties can be explained based on the microstrain within the nanolaminated structure, and crosslinking of the boron chains with the rest of the structure. The changes in the boron chains lead to much weaker bonds between them and the surrounding metal atoms and to degradation of the overall elastic properties at x ratios > 0.375. The addition of Nb into Mo_2BC was predicted to decrease its ductility in the whole composition range. Calculated mixing enthalpy of the solid solution shows that the solid solutions are unlikely to decompose into Mo_2BC and Nb_2BC in the range of x ratios up to 0.375, whereas the stability decreases at x ratios larger than 0.375.

A series of $(Mo_{1-x}Nb_x)_2BC$ thin films were deposited by combinatorial magnetron sputtering covering the full compositional range between and including Mo_2BC and Nb_2BC to verify the predicted trends. The measured effective modulus accurately reproduced the predicted non-linear trend with the maximum of the effective elastic modulus in the compositional region close to $x = 0.25$. The measured effective modulus was lower than the calculated one due to the low crystallinity of the coatings with sub−10 nm grain size and amorphous regions in the coating at the column walls.

Addendum — TEM investigation of orthorhombic and fcc phases

The observed diffraction rings for Mo_2BC shown in Fig. 14 are listed in Table 1. The SAED of Nb_2BC and $(Mo_{1-x}Nb_x)_2BC$ phases with $x = 0.25$ can be indexed as fcc structure. If one considers only the strong reflections of Mo_2BC, the SAED pattern of Mo_2BC also can be indexed as an fcc phase, which has a 111-preferred orientation. However, if we want to interpret all the reflections of Mo_2BC, the structure of orthorhombic Mo_2BC (PDF Card No.: 00-029-0913) seems a proper choice. Mo_2BC can be better indexed as orthorhombic Mo_2BC. However, its strong reflections (bold characters in Table 1 and strong lines in Fig. 14) coincide with allowed reflections of the fcc structure, and weak reflections coincide with cubic reflections forbidden in the fcc system. This orthorhombic structure was proposed by Jeitschko et al. in 1963 [1]. The creators of the unit cell have already remarked that "the shape of the cell reveals a certain resemblance to MoB type; the reflex system also indicates the existence of pseudocubic sub cell". From the relation of cell parameters of the orthorhombic and cubic structure, the following relation can be recognized: the two short sides of the orthorhombic cell are almost equal and are $\sim a_0/\sqrt{2}$ ($= a_{110}$ of cubic lattice), while the long side is $\sim 4 \cdot a_0$, where a_0 is the parameter of cubic cell. Therefore, the orthorhombic cell can be interpreted as a supercell generated from the fcc cell. The orthorhombic phase contains altering

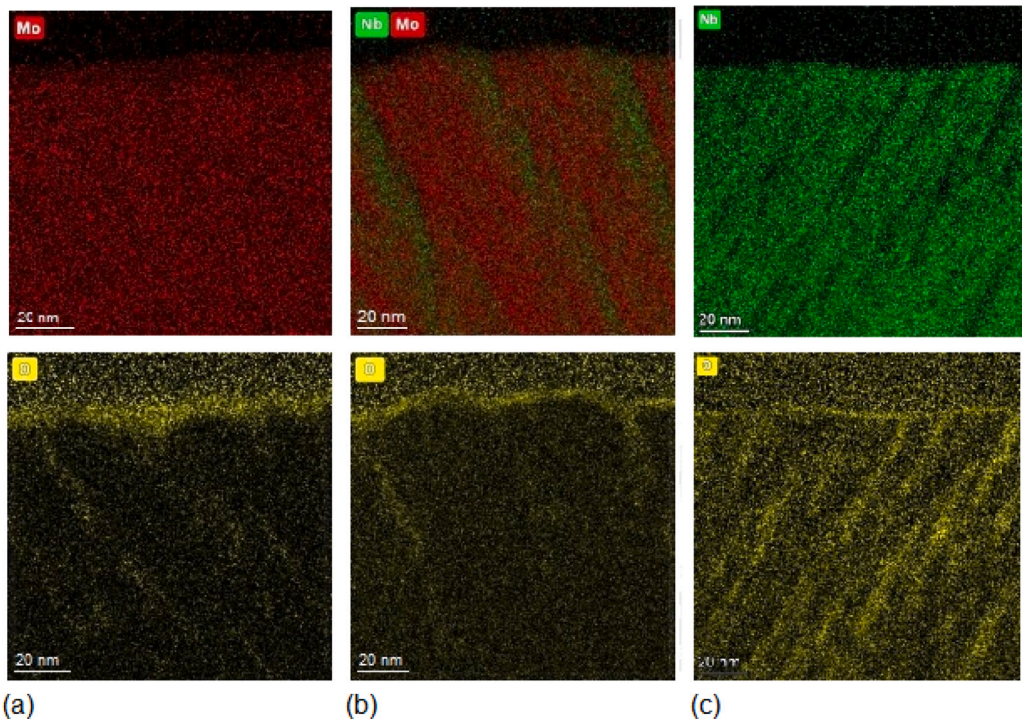

Fig. 11. EDX elemental maps of Mo_2BC (a), $(Mo_{1-x}Nb_x)_2BC$ with x = 0.25 (b) and of Nb_2BC (c) showing Nb and Mo (top) and O (bottom).

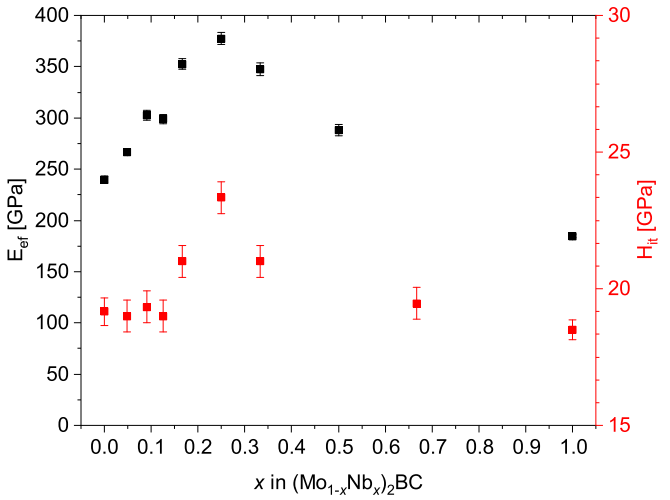

Fig. 12. The effective elastic modulus E_{ef} and the indentation hardness H_{it} as functions of x in $(Mo_xNb_{1-x})_2BC$.

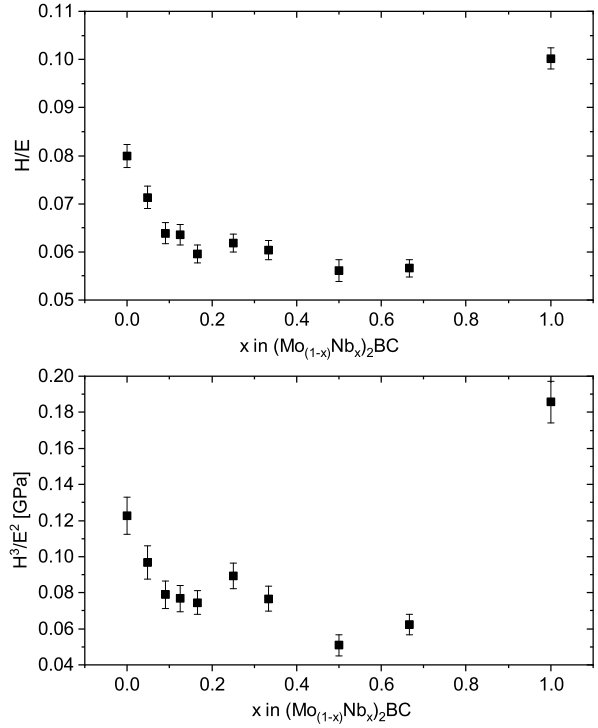

Fig. 13. H/E and H^3/E^2 ratios as functions of x in $(Mo_xNb_{1-x})_2BC$.

planes containing stiff carbidic and boridic bonds with a high degree of ionicity and weaker metallic planes. Within the orthorhombic unit cell, the arrangement of heavy metal atoms (Mo, Nb) preserves a cubic (fcc) arrangement characteristic for cubic transition metal carbides. The non-random positions of the light elements (B and C) on the carbon positions of cubic carbide structure create the special orthorhombic unit cell. Due to the low scattering power of the light elements, this ordering has a weak effect on the diffraction pattern, i.e. some weak reflections appear in addition to the strong fcc pattern. Consequently, cubic and orthorhombic structures may not be distinguished for very small grain sizes. However, this is not exclusively a technical question. Unambiguous distinction between fcc and orthorhombic structure may be elusive for very small grains because structural elements with cubic ordering are precursors of the orthorhombic supercell. This may be the case for Nb_2BC sample, where minor deviations of diffraction reflections from the cubic system may indicate the onset of medium scale ordering. In the Nb_2BC and Mo_2BC samples, the 111 spacing (cubic notation) is 1.7 and is 2% higher than the value calculated from the lattice parameter. Similarly, the 311 spacing of Nb_2BC is about 1% higher than calculated from fcc structure. This can be an indication that

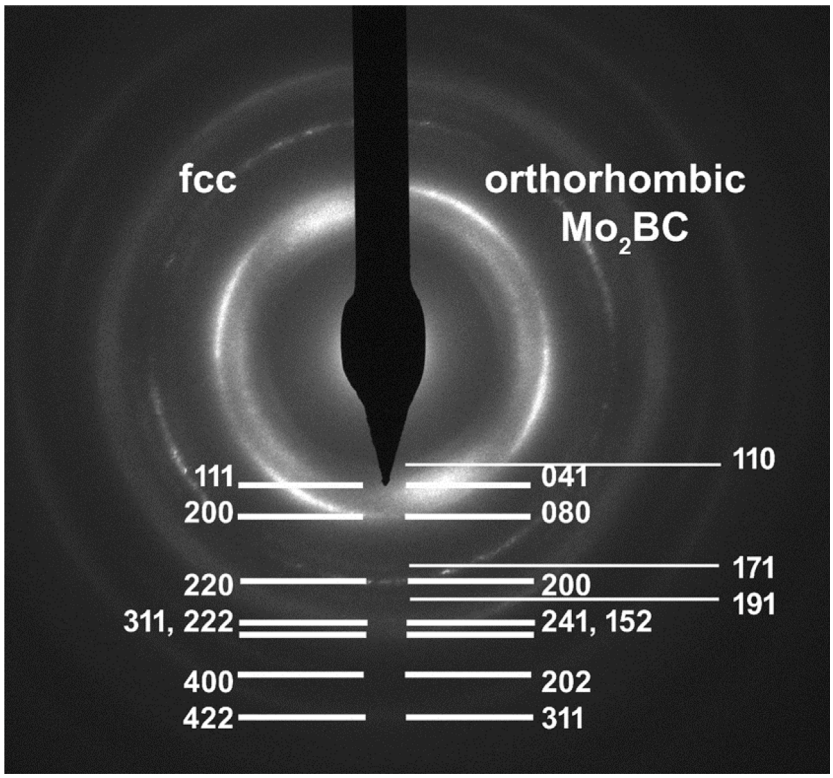

Fig. 14. SAED pattern of the Mo_2BC coating. Coincidences of strong reflections of orthorhombic Mo_2BC (PDF Card No.: 00-029-0913) with reflections of cubic (fcc) structure are indicated. In addition to the coinciding strong reflections, some weak diffraction rings can be identified, confirming the formation of an orthorhombic structure. The fcc notation can be applied to the SAED patterns of the other two $(Mo_{1-x}Nb_x)_2BC$ phases with $x = 0$ and $x = 0.25$.

Table 1
The observed SAED rings of $(Mo_{1-x}Nb_x)_2BC$ samples with $x = 0$, 0.25 and 1. The rings of samples $x = 0$ and 0.25 can be indexed as an fcc structure. The Miller indices highlighted by bold characters are the allowed reflections in fcc. Mo_2BC can be better indexed as orthorhombic Mo_2BC. However, its strong reflections (highlighted by bold characters in column 5) coincide with reflections of fcc structure, and weak reflections coincide with reflections that are forbidden in the fcc structure or do not exist in the cubic system (like $h^2 + k^2 + l^2 = 7$). Values in parentheses from XRD measurements are added for comparison where applicable.

Cubic					Orthorhombic
$h^2+k^2+l^2$	Miller indices	$(Mo_{1-x}Nb_x)_2BC$ $x = 0$	$(Mo_{1-x}Nb_x)_2BC$ $x = 0.25$	$(Mo_{1-x}Nb_x)_2BC$ $x = 1$	
		(fcc a_0 = 4.43)	(fcc a_0 = 4.375)	(cubic a_0 = 4.37)	*hkl* (PDF Card No.: 00-029-0913)
2	110			3.033 Å	110
3	**111**	**2.599** Å (2.50 Å)	**2.514** Å	**2.468** Å (2.61 Å)	041+130,150
4	**200**	**2.214** Å (2.17 Å)	**2.195** Å	**2.168** Å (2.22 Å)	080, 111
7	–			1.650 Å	171
8	**220**	**1.569** Å (1.55 Å)	**1.558** Å	**1.544** Å (1.57 Å)	200
9	300, 221			1.434 Å	191
11	**311**	**1.351** Å	**1.323** Å	**1.317** Å (1.35 Å)	241
12	**222**	**1.286** Å	**1.272** Å	**1.266** Å (1.28 Å)	152, 280, 082
16	**400**	**1.111** Å	**1.093** Å	1.09 Å	202
20	**420**	**0.995** Å	**0.983** Å	0.975 Å	311, 282

there is a certain orthorhombic ordering present also in Nb_2BC, like for Mo_2BC (Table 1). However, it cannot be unambiguously identified.

Declaration of competing interest

The authors declare that they have no known competing financial interests or personal relationships that could have appeared to influence the work reported in this paper.

Acknowledgements

This work was supported by the project LM2023039 and e-INFRA CZ (ID: 90254) funded by the Ministry of Education, Youth and Sports of the Czech Republic and from Operational Programme Research, Development and Education - Project "MSCAfellow5_MUNI" (No. CZ.02.01.01/00/22_010/0003229). The microstructural characterization (TEM) was supported by grant no. VEKOP-2.3.3-15-2016-00002 and VEKOP-2.3.2-16-2016-00011 of the European Structural and Investment Funds. Personal meetings and discussions with foreign co-authors were facilitated by means of the Czech and Austrian mobility programs 8J21AT013 and OeAD-WTZ CZ 08/2021.

Appendix A. Supplementary data

Supplementary material related to this article can be found online at https://doi.org/10.1016/j.actamat.2024.119741.

References

[1] W. Jeitschko, H. Nowotny, F. Benesovsky, Die Kristallstruktur von Mo_2BC, Monatsh Chem. Verw Tl 94 (3) (1963) 565–568, http://dx.doi.org/10.1007/BF00903497.

[2] L. Toth, High superconducting transition temperatures in the molybdenum carbide family of compounds, J. Less-Common Met. 13 (1) (1967) 129–131, http://dx.doi.org/10.1016/0022-5088(67)90055-0.

[3] G. Smith, A. Tharp, Q. Johnson, Determination of the light-atom positions in Mo_2BC, Acta Crystall. B-Stru. 25 (4) (1969) 698–701, http://dx.doi.org/10.1107/S0567740869002846.

[4] J.-O. Bovin, M. O'Keeffe, L. Stenberg, Planar defects in Mo_2BC. An electron microscope study, J. Solid State Chem. 22 (2) (1977) 221–231, http://dx.doi.org/10.1016/0022-4596(77)90041-X.

[5] H. Holleck, Material selection for hard coatings, J. Vac. Sci. Technol. A 4 (6) (1986) 2661–2669, http://dx.doi.org/10.1116/1.573700.

[6] H. Holleck, Basic principles of specific applications of ceramic materials as protective layers, Surf. Coat. Technol. 43 (1990) 245–258, http://dx.doi.org/10.1016/0257-8972(90)90078-q.

[7] C. Mitterer, M. Rauter, P. Rödhammer, Sputter deposition of ultrahard coatings within the system Ti-B-C-N, Surf. Coat. Technol. 41 (3) (1990) 351–363, http://dx.doi.org/10.1016/0257-8972(90)90146-4.

[8] J. Emmerlich, D. Music, M. Braun, P. Fayek, F. Munnik, J.M. Schneider, A proposal for an unusually stiff and moderately ductile hard coating material: Mo_2BC, J.Phys. D Appl. Phys. 42 (18) (2009) 185406, http://dx.doi.org/10.1088/0022-3727/42/18/185406.

[9] P. Souček, L. Zábranský, V. Buršíková, J. Buršík, S. Debnárová, M. Svoboda, V. Peřina, P. Vašina, Fracture resistance enhancement in hard Mo-B-C coatings tailored by composition and microstructure, J. Nanomater. 2018 (2018) http://dx.doi.org/10.1155/2018/5184584.

[10] P. Malinovskis, J. Palisaitis, P.A. Persson, U. Jansson, E. Lewin, Synthesis and characterisation of Mo-B-C thin films deposited by non-reactive DC magnetron sputtering, Surf. Coat. Technol. 309 (2017) 506–515, http://dx.doi.org/10.1016/j.surfcoat.2016.12.003.

[11] L. Zábranský, V. Buršíková, P. Souček, P. Vašina, J. Dugáček, P. St'ahel, J. Buršík, M. Svoboda, V. Peřina, Thermal stability of hard nanocomposite Mo-B-C coatings, Vacuum 138 (2017) 199–204, http://dx.doi.org/10.1016/j.vacuum.2016.12.016.

[12] H. Bolvardi, J. Emmerlich, S. Mráz, M. Arndt, H. Rudigier, J.M. Schneider, Low temperature synthesis of Mo_2BC thin films, Thin Solid Films 542 (2013) 5–7, http://dx.doi.org/10.1016/j.tsf.2013.07.021.

[13] H. Bolvardi, J. Emmerlich, D. Music, J. von Appen, R. Dronskowski, J.M. Schneider, Systematic study on the electronic structure and mechanical properties of X_2BC (X=Mo, Ti, V, Zr, Nb, Hf, Ta and W), J. Phys.-Condens. Mat. 25 (4) (2012) 045501, http://dx.doi.org/10.1088/0953-8984/25/4/045501.

[14] M. Friedemann, H. Klostermann, Composition and mechanical properties of B-C-W and B-C-Ti thin films prepared by pulse magnetron sputtering, Surf. Coat. Technol. 308 (2016) 115–120, http://dx.doi.org/10.1016/j.surfcoat.2016.07.107.

[15] M. Alishahi, S. Mirzaei, P. Souček, L. Zábranský, V. Buršíková, M. Stupavská, V. Peřina, K. Balázsi, Zs. Czigány, P. Vašina, Evolution of structure and mechanical properties of hard yet fracture resistant W-B-C coatings with varying C/W ratio, Surf. Coat. Technol. 340 (2018) 103–111, http://dx.doi.org/10.1016/j.surfcoat.2018.02.054.

[16] S. Mirzaei, M. Alishahi, P. Souček, L. Zábranský, V. Buršíková, M. Stupavská, V. Peřina, K. Balázsi, Zs. Czigány, P. Vašina, Effect of bonding structure on hardness and fracture resistance of W-B-C coatings with varying B/W ratio, Surf. Coat. Technol. 358 (2019) 843–849, http://dx.doi.org/10.1016/j.surfcoat.2018.12.007.

[17] M. Kroker, P. Souček, L. Zábranský, V. Buršíková, Zs. Czigány, V. Sochora, K. Balázsi, M. Jílek, P. Vašina, Industrially deposited hard and damage resistant W-B-C coatings, Surf. Coat. Technol. 454 (2023) 129150, http://dx.doi.org/10.1016/j.surfcoat.2022.129150.

[18] N. Nedfors, O. Tengstrand, P. Eklund, L. Hultman, U. Jansson, Nb-B-C thin films for electrical contact applications deposited by magnetron sputtering, J. Vac. Sci. Technol. A 32 (4) (2014) 041503, http://dx.doi.org/10.1116/1.4875135.

[19] S. Debnárová, P. Souček, V. Buršíková, M. Hans, D.M. Holzapfel, S. Mráz, J.M. Schneider, P. Vašina, Phase formation, thermal stability and mechanical properties of Nb-B-C coatings prepared by combinatorial magnetron sputtering, Surf. Coat. Technol. 433 (2022) 128137, http://dx.doi.org/10.1016/j.surfcoat.2022.128137.

[20] S. Debnárová, P. Souček, P. Ondračka, D. Holzapfel, S. Mráz, J.M. Schneider, P. Vašina, Phase formation of powders sputtered from X_2BC targets and XC+XB powder mixtures {X=Nb, Ta, W}, Surf. Coat. Technol. 458 (2023) 129379, http://dx.doi.org/10.1016/j.surfcoat.2023.129379.

[21] M. Polaček, P. Souček, M. Alishahi, N. Koutná, P. Klein, L. Zábranský, Zs. Czigány, K. Balázsi, P. Vašina, Synthesis and characterization of Ta-B-C coatings prepared by DCMS and HiPIMS co-sputtering, Vacuum 199 (2022) 110937, http://dx.doi.org/10.1016/j.vacuum.2022.110937.

[22] W. Kohn, L.J. Sham, Self-consistent equations including exchange and correlation effects, Phys. Rev. 140 (4A) (1965) A1133, http://dx.doi.org/10.1103/physrev.140.a1133.

[23] P. Hohenberg, W. Kohn, Inhomogeneous electron gas, Phys. Rev. 136 (3B) (1964) B864, http://dx.doi.org/10.1103/physrev.136.b864.

[24] P. Giannozzi, S. Baroni, N. Bonini, M. Calandra, R. Car, C. Cavazzoni, D. Ceresoli, G.L. Chiarotti, M. Cococcioni, I. Dabo, A. Dal Corso, S. de Gironcoli, S. Fabris, G. Fratesi, R. Gebauer, U. Gerstmann, C. Gougoussis, A. Kokalj, M. Lazzeri, L. Martin-Samos, N. Marzari, F. Mauri, R. Mazzarello, S. Paolini, A. Pasquarello, L. Paulatto, C. Sbraccia, S. Scandolo, G. Sclauzero, A.P. Seitsonen, A. Smogunov, P. Umari, R.M. Wentzcovitch, QUANTUM ESPRESSO: a modular and open-source software project for quantum simulations of materials, J. Phys.-Condens. Mat. 21 (39) (2009) 395502, http://dx.doi.org/10.1088/0953-8984/21/39/395502.

[25] P. Giannozzi, O. Andreussi, T. Brumme, O. Bunau, M. Buongiorno Nardelli, M. Calandra, R. Car, C. Cavazzoni, D. Ceresoli, M. Cococcioni, N. Colonna, I. Carnimeo, A. Dal Corso, S. de Gironcoli, P. Delugas, R.A. DiStasio, A. Ferretti, A. Floris, G. Fratesi, G. Fugallo, R. Gebauer, U. Gerstmann, F. Giustino, T. Gorni, J. Jia, M. Kawamura, H.-Y. Ko, A. Kokalj, E. Küçükbenli, M. Lazzeri, M. Marsili, N. Marzari, F. Mauri, N.L. Nguyen, H.-V. Nguyen, A. Otero-de-la Roza, L. Paulatto, S. Poncé, D. Rocca, R. Sabatini, B. Santra, M. Schlipf, A.P. Seitsonen, A. Smogunov, I. Timrov, T. Thonhauser, P. Umari, N. Vast, X. Wu, S. Baroni, Advanced capabilities for materials modelling with QUANTUM ESPRESSO, J. Phys.-Condens. Mat. 29 (46) (2017) 465901, http://dx.doi.org/10.1088/1361-648x/aa8f79.

[26] A. Zunger, S.-H. Wei, L. Ferreira, J.E. Bernard, Special quasirandom structures, Phys. Rev. Lett. 65 (3) (1990) 353, http://dx.doi.org/10.1103/physrevlett.65.353.

[27] D. Gehringer, M. Friák, D. Holec, Models of configurationally-complex alloys made simple, Comput. Phys. Comm. 286 (2023) 108664, http://dx.doi.org/10.1016/j.cpc.2023.108664.

[28] G. Prandini, A. Marrazzo, I.E. Castelli, N. Mounet, N. Marzari, Precision and efficiency in solid-state pseudopotential calculations, npj Comp. Mater. 4 (1) (2018) 72, http://dx.doi.org/10.1038/s41524-018-0127-2.

[29] K. Lejaeghere, G. Bihlmayer, T. Björkman, P. Blaha, S. Blügel, V. Blum, D. Caliste, I.E. Castelli, S.J. Clark, A. Dal Corso, S. de Gironcoli, T. Deutsch, J.K. Dewhurst, I. Di Marco, C. Draxl, M. Dułak, O. Eriksson, J.A. Flores-Livas, K.F. Garrity, L. Genovese, P. Giannozzi, M. Giantomassi, S. Goedecker, X. Gonze, O. Grånäs, E.K.U. Gross, A. Gulans, F. Gygi, D.R. Hamann, P.J. Hasnip, N.A.W. Holzwarth, D. Iuşan, D.B. Jochym, F. Jollet, D. Jones, G. Kresse, K. Koepernik, E. Küçükbenli, Y.O. Kvashnin, I.L.M. Locht, S. Lubeck, M. Marsman, N. Marzari, U. Nitzsche, L. Nordström, T. Ozaki, L. Paulatto, C.J. Pickard, W. Poelmans, M.I.J. Probert, K. Refson, M. Richter, G.-M. Rignanese, S. Saha, M. Scheffler, M. Schlipf, K. Schwarz, S. Sharma, F. Tavazza, P. Thunström, A. Tkatchenko, M. Torrent, D. Vanderbilt, M.J. van Setten, V. Van Speybroeck, J.M. Wills, J.R. Yates, G.-X. Zhang, S. Cottenier, Reproducibility in density functional theory calculations of solids, Science 351 (6280) (2016) aad3000, http://dx.doi.org/10.1126/science.aad3000.

[30] D. Hamann, Optimized norm-conserving Vanderbilt pseudopotentials, Phys. Rev. B 88 (8) (2013) 085117, http://dx.doi.org/10.1103/physrevb.88.085117.

[31] A. Dal Corso, Pseudopotentials periodic table: From H to Pu, Comput. Mater. Sci. 95 (2014) 337–350, http://dx.doi.org/10.1016/j.commatsci.2014.07.043.

[32] K.F. Garrity, J.W. Bennett, K.M. Rabe, D. Vanderbilt, Pseudopotentials for high-throughput DFT calculations, Comput. Mater. Sci. 81 (2014) 446–452, http://dx.doi.org/10.1016/j.commatsci.2013.08.053.

[33] J.P. Perdew, A. Ruzsinszky, G.I. Csonka, O.A. Vydrov, G.E. Scuseria, L.A. Constantin, X. Zhou, K. Burke, Restoring the density-gradient expansion for exchange in solids and surfaces, Phys. Rev. Lett. 100 (13) (2008) 136406, http://dx.doi.org/10.1103/physrevlett.100.136406.

[34] R. Yu, J. Zhu, H. Ye, Calculations of single-crystal elastic constants made simple, Comput. Phys. Comm. 181 (3) (2010) 671–675, http://dx.doi.org/10.1016/j.cpc.2009.11.017.

[35] R. Hill, The elastic behaviour of a crystalline aggregate, P. Phys. Soc. A 65 (5) (1952) 349, http://dx.doi.org/10.1088/0370-1298/65/5/307.

[36] R. Gaillac, P. Pullumbi, F.-X. Coudert, ELATE: an open-source online application for analysis and visualization of elastic tensors, J. Phys.-Condens. Mat. 28 (27) (2016) 275201, http://dx.doi.org/10.1088/0953-8984/28/27/275201.

[37] S. Maintz, V.L. Deringer, A.L. Tchougréeff, R. Dronskowski, LOBSTER: A tool to extract chemical bonding from plane-wave based DFT, J. Comput. Chem. 37 (11) (2016) 1030–1035, http://dx.doi.org/10.1002/jcc.24300.

[38] R. Dronskowski, P.E. Blöchl, Crystal orbital hamilton populations (COHP): energy-resolved visualization of chemical bonding in solids based on density-functional calculations, J. Phys. Chem. 97 (33) (1993) 8617–8624, http://dx.doi.org/10.1021/j100135a014.

[39] P. Ondračka, NOMAD dataset: Effect of Nb incorporation in Mo_2BC coatings on structural and mechanical properties - ab initio modeling and experiment - ab initio data, 2023, http://dx.doi.org/10.17172/NOMAD/2023.10.02-1.

[40] C. Draxl, M. Scheffler, NOMAD: The FAIR concept for big data-driven materials science, MRS Bull. 43 (9) (2018) 676–682, http://dx.doi.org/10.1557/mrs.2018.208.

[41] M. Scheidgen, L. Himanen, A.N. Ladines, D. Sikter, M. Nakhaee, Á. Fekete, T. Chang, A. Golparvar, J.A. Márquez, S. Brockhauser, S. Brückner, L.M. Ghiringhelli, F. Dietrich, D. Lehmberg, T. Denell, A. Albino, H. Näsström, S. Shabih, F. Dobener, M. Kühbach, R. Mozumder, J.F. Rudzinski, N. Daelman, J.M.

Pizarro, M. Kuban, C. Salazar, P. Ondračka, H.-J. Bungartz, C. Draxl, NOMAD: A distributed web-based platform for managing materials science research data, J. Open Source Softw. 8 (90) (2023) 5388, http://dx.doi.org/10.21105/joss.05388.

[42] J.L. Lábár, M. Adamik, B. Barna, Zs. Czigány, Zs. Fogarassy, Z.E. Horváth, O. Geszti, F. Misják, J. Morgiel, G. Radnóczi, G. Sáfrán, L. Székely, T. Szüts, Electron diffraction based analysis of phase fractions and texture in nanocrystalline thin films, part III: Application examples, Microsc. Microanal. 18 (2) (2012) 406–420, http://dx.doi.org/10.1017/s1431927611012803.

[43] W.C. Oliver, G.M. Pharr, An improved technique for determining hardness and elastic modulus using load and displacement sensing indentation experiments, J. Mater. Res. 7 (6) (1992) 1564–1583, http://dx.doi.org/10.1557/jmr.1992.1564.

[44] K. Momma, F. Izumi, VESTA 3 for three-dimensional visualization of crystal, volumetric and morphology data, J. Appl. Crystallogr. 44 (6) (2011) 1272–1276, http://dx.doi.org/10.1107/s0021889811038970.

[45] R. Dronskowski, P.E. Bloechl, Crystal orbital hamilton populations (COHP): energy-resolved visualization of chemical bonding in solids based on density-functional calculations, J. Phys. Chem. 97 (33) (1993) 8617–8624, http://dx.doi.org/10.1021/j100135a014.

[46] A.M. Tehrani, A. Lim, J. Brgoch, Mechanism for unconventional nonlinear elasticity, Phys. Rev. B 100 (6) (2019) 060102, http://dx.doi.org/10.1103/physrevb.100.060102.

[47] A. Jain, S.P. Ong, G. Hautier, W. Chen, W.D. Richards, S. Dacek, S. Cholia, D. Gunter, D. Skinner, G. Ceder, K.A. Persson, Commentary: The materials project: A materials genome approach to accelerating materials innovation, APL Mater. 1 (1) (2013) http://dx.doi.org/10.1063/1.4812323.

[48] D. Holec, R. Rachbauer, L. Chen, L. Wang, D. Luef, P.H. Mayrhofer, Phase stability and alloy-related trends in Ti-Al-N, Zr-Al-N and Hf-Al-N systems from first principles, Surf. Coat. Technol. 206 (7) (2011) 1698–1704, http://dx.doi.org/10.1016/j.surfcoat.2011.09.019.

[49] M. Kroker, Zs. Czigány, Z. Weiss, M. Fekete, P. Souček, K. Balázsi, V. Sochora, M. Jílek, P. Vašina, On the origin of multilayered structure of W-B-C coatings prepared by non-reactive magnetron sputtering from a single segmented target, Surf. Coat. Technol. 377 (2019) 124864, http://dx.doi.org/10.1016/j.surfcoat.2019.07.077.

[50] M.G.D.V. Cuppari, S.F. Santos, Physical properties of the NbC carbide, Metals 6 (10) (2016) 250, http://dx.doi.org/10.3390/met6100250.

[51] A. Bahr, T. Glechner, T. Wojcik, A. Kirnbauer, M. Sauer, A. Foelske, O. Hunold, J. Ramm, S. Kolozsvári, E. Ntemou, E. Pitthan, D. Primetzhofer, H. Riedl, N. Hahn, Non-reactive HiPIMS deposition of NbC_x thin films: Effect of the target power density on structure-mechanical properties, Surf. Coat. Technol. 444 (2022) 128674, http://dx.doi.org/10.1016/j.surfcoat.2022.128674.

[52] N. Sala, M.D. Abad, J.C. Sánchez-López, M. Cruz, J. Caro, C. Colominas, Tribological performance of Nb-C thin films prepared by DC and HiPIMS, Mater. Lett. 277 (2020) 128334, http://dx.doi.org/10.1016/j.matlet.2020.128334.

[53] C.E. Carlton, P.J. Ferreira, What is behind the inverse Hall–Petch effect in nanocrystalline materials? Acta Mater. 55 (11) (2007) 3749–3756, http://dx.doi.org/10.1016/j.actamat.2007.02.021.

[54] A. Leyland, A. Matthews, On the significance of the H/E ratio in wear control: A nanocomposite coating approach to optimised tribological behaviour, Wear 246 (1–2) (2000) 1–11, http://dx.doi.org/10.1016/s0043-1648(00)00488-9.

[55] J. Musil, F. Kunc, H. Zeman, H. Poláková, Relationships between hardness, Young's modulus and elastic recovery in hard nanocomposite coatings, Surf. Coat. Technol. 154 (2–3) (2002) 304–313, http://dx.doi.org/10.1016/s0257-8972(01)01714-5.

[56] Y.T. Pei, D. Galvan, J.Th.M. De Hosson, A. Cavaleiro, Nanostructured TiC/a-C coatings for low friction and wear resistant applications, Surf. Coat. Technol. 198 (1–3) (2005) 44–50, http://dx.doi.org/10.1016/j.surfcoat.2004.10.106.